Integrative Biology, 2024, **16**, zyae016
https://doi.org/10.1093/intbio/zyae016
Original Article

Delayed jamming-induced oscillatory migration patterns of epithelial collectives under long-range confinement

S. Lohmann[1,†], F.M. Pramotton[1,2,3,†], A. Taloni[4,†], A. Ferrari[1,3], D. Poulikakos[1], C. Giampietro[2,3,*]

[1]Laboratory of Thermodynamics in Emerging Technologies, DMAVT, ETH Zürich, Sonneggstr 3, 8092, Zürich, Switzerland
[2]Experimental Continuum Mechanics, DMAVT, ETH Zürich, Leonhardstr. 21, 8092, Zürich, Switzerland
[3]Empa, Materials Science and Technology, Überlandstrasse 129, 8600, Dübendorf, Switzerland
[4]ISC Institute for complex systems - National Research Council of Italy, P.le Aldo Moro 5, 00185, Roma, Italy

*Corresponding author. Laboratory of cell mechanics and mechanobiology, ECM group, Empa, Überlandstrasse 129, 8600, Dübendorf, Switzerland, Email: costanza.giampietro@empa.ch
†Lohmann, Pramotton and Taloni contributed equally to this work. They all are co-first authors.

Abstract

Collective dynamics of cells in confined geometry regulate several biological processes including cell migration, proliferation, differentiation, and communication. In this work, combining simulation with experimental data, we studied the oscillatory motion of epithelial sheets in smaller areas of confinement, and we linked the monolayer maturation induced-jamming with the wave formation. We showed that epithelial cell populations with delayed jamming properties use the additional time available from this delay to coordinate their movement, generating wave motion in larger areas of confinement compared to control populations. Furthermore, the effects of combining geometric confinement with contact guiding micro-gratings on this wave formation were investigated. We demonstrated that collective migratory oscillations under large geometrical confinement depend on the jamming state of the cell monolayers. The early dynamical state of the experimental results obtained was simulated by self-propelled Voronoi computations, comparing cells with solid-like and fluid-like behavior. Together our model describes the wave formation under confinement and the nodal oscillatory dynamics of the early dynamic stage of the system.

INSIGHT BOX
Collective behavior of cells in confined spaces impacts biological processes. Through experimental data combined with simulations, the oscillatory motion of epithelial sheets in small areas of confinement was described. A correlation between the level of cell jamming and the formation of waves was detected. Cell populations with delayed jamming presented wave motion in larger confinement areas. The effects of combining geometric confinement with substrate micro-gratings demonstrated that the collective migratory oscillations in large confinement areas rely on the jamming state of cells. The early dynamical state was simulated using self-propelled Voronoi computations that help to understand wave formation under confinement and the nodal oscillatory dynamics of early-stage systems.

Keywords: collective cell motion; geometric confinement; oscillatory dynamics

Introduction

Collective dynamics of cells play important roles in tissue formation, adaptation, and repair [1–3]. Collective cell motion relies on cellular interactions ensured by junction complexes, which physically link individual cells, enabling rapid intercellular communication and coordination of movement across many cells [4–7]. As a result, cellular sheets behave as a supra-cellular contractile network, which responds in a coordinated fashion to external and internal mechanical cues [8, 9]. It was previously reported that collective migration occurs through the transfer of mechanical information between cells. The alignment of cell velocity and mechanical stress (plithotaxis) is crucial for inducing coordinated migration [10]. Collective cell behavior, such as collective motion (migration), is also influenced by mechanical boundary conditions imposed by geometrical confinements [11–13], which impact on tissue development and adaptation, by controlling cell morphology and gene expression [14, 15]. Indeed, *in vivo*, cells are always subjected to geometric constraints from their base membrane or the surrounding tissue. For example, in drosophila embryogenesis, a geometric fold is required to maintain mechanical balance within the epithelial cell sheet and permits correct embryonic development [16, 17]. Consequently, when injury or disease modify geometric constraints, cell movement is impacted, contributing to the aggravation of pathological development. Neural crest cells depend on a geometric boundary from surrounding cells to guide elongation, and loss thereof leads to faulty formation of the neural crest [18]. Furthermore, geometric confinement

Received: February 14, 2024. **Revised:** September 11, 2024. **Accepted:** September 18, 2024

plays a key role in triggering cancer cell invasion [19]. Cancer cells align with confining extracellular matrix (ECM) fibers, which thereby guide cancer invasion [20] and determine cell migration velocity through their density [21].

During the initial phase of monolayer formation, as is the case in morphogenesis *in vivo* or after placing cells on a substrate *in vitro*, cells exhibit high degrees of motion [22]. This state of motion is referred to as the unjammed state, characterized by the ability of cells to exchange neighbors [23, 24]. In mature epithelial monolayers, collective motion ends when cells jam due to increased cell density and the maturation of cell–cell junctions [25]. However, cells retain the ability to unjam and collectively migrate during situations of development, adaptation, and repair, such as morphogenesis and wound healing [26]. Following disruption of a cell monolayer during *in vitro* wound healing, propagating waves of coordinated migration emerge away from the wound edge and disintegrate near the advancing front [27]. Furthermore, in certain pathological conditions like asthma, epithelial monolayers remain in a sustained unjammed state [22]. In the unjammed state, monolayer-forming cells move in flocks or swirls, coordinating their direction of movement over a characteristic length scale defined as the velocity correlation length [28, 29].

When cells are confined at the scale of their correlation length or below, coordination of movement leads to coherent rotations in circular or square confinements [30–32], and multi-nodal oscillations in high aspect-ratio rectangular confinements [33]. In circular confinements larger than the velocity correlation length, cells continue to move as a flocking liquid in transient rather than sustained oscillations [32, 34]. However, so far, studies of collective migration under confinement are generally restricted to the initial, unjammed phase of epithelial monolayer formation, and insights into the coherence of jamming and migration under confinement are therefore limited. In addition, it is well established that epithelial cells are guided by several chemical and mechanical cues. Both *in vivo* and *in vitro*, properties of the base tissue or substrate, such as rigidity (durotaxis), adhesiveness (haptotaxis), and microtopography (contact guidance), are known to direct cell motion [35, 36]. In tissue development and adaptation, these guidance mechanisms do not act in isolation but coincide with tissue confinement [37]. Therefore, understanding the interplay between mechanical guidance cues and cellular confinement is crucial to further elucidate collective cellular migration.

Here we combined experimental data and simulations to describe the oscillatory motion of epithelial sheets in small areas of confinement. We identified a correlation between the level of cell jamming and the formation of waves. Together, our work offers new insights into the induction of waves of cells that move coordinately during collective cell migration under confinement.

Materials and methods

Cell culture

MDCK WT and PM-YFP cells [38, 39] were cultured in Dulbecco's modified Eagle's medium-high glucose media (Sigma-Aldrich) supplemented with 10% fetal bovine serum (FBS, Sigma-Aldrich), 100 U = ml PenStrep (LifeScience), and 2×10^{-3} mmol L-glutamine (LifeScience). MCF-10A EV and MCF10ARab5 cells were a kind gift of Prof. Giorgio Scita (IFOM - Milano) and were maintained in DMEM/F12 medium (Invitrogen) supplemented with 5% horse serum, 0.5 mg/ml hydrocortisone, 100 ng/ml cholera toxin, 10 μg/ml insulin and 20 ng/ml EGF [40]. All cell lines were grown at 37°C in humidified atmosphere with 5% CO2. In all the experiments a total of 8×104 cells/cm2 were seeded on substrates.

Substrate fabrication

Gratings with groove depth and width of 1 μm and duty cycle of 2 μm were imprinted on 180 μm thick Cyclic Olefin Copolymer foils (COC, Ibidi) using nano-imprint lithography, as previously reported [41]. Oxygen plasma treatment (80 W for 60 s, 1 ± 0.2 mbar) was performed to clean the substrates and increase their hydrophilicity.

Stencil fabrication

The molds used for the fabrication of the stencils were designed on Autodesk Inventor Professional and then printed with the Object 500 Connex 3 3-D printer, the material used was Vero White Plus. Stencils comprised polydimethylsiloxane (PDMS, Dow Corning) prepared by mixing PDMS at 1:10 ratio. Briefly, the PDMS was degassed in a vacuum chamber and immediately poured into the mold. The solution was then briefly degassed for a second time and then cured for 2 h at 80°C. The resulting stencils were carefully separated from the mold. Before the experiments, the stencils were routinely cleaned in 70% ethanol for 10 min and air-dried. Last, a treatment with Pluronic F127 (Sigma-Aldrich) for 2 h to enable cell attachment on the lateral walls during experiments.

PDMS bonding

The COC microstructure substrates were mounted at the bottom of hollowed wells in 6-well plates and both COC structures and stencil were oxygen plasma treated (80 W for 60 s, 1 ± 0.2 mbar) to increase their hydrophilicity. Stencils were gently positioned on the substrates to allow the bonding. To enhance the bonding efficacy the mounted PDMS-COC substrate was cured in the oven at 65°C for 20 min. The resulting substrates were coated with 15 μg/ml fibronectin (Sigma-Aldrich).

Cell microscopy

Cell movement was detected using an inverted Nikon-Ti wide-field microscope (Nikon, Japan) and an incubation chamber (Life Imaging Services, Switzerland). The medium was maintained at a controlled temperature of 37°C and CO_2 concentration of 5%. Time-lapse experiments were set to routinely collect images, in different spatial positions of the sample, in the bright field (BF) channel with a time resolution of 15 min and 30 min with a 20×, 0.45 NA long-distance objective (Plan Fluor, Nikon, Japan).

Velocity measurement

Cell image velocimetry (CIV) toolbox was used for the analysis of time series as previously described [42]. The velocity field provided by the CIV analysis was quantified by the mean cell layer speed (mean velocity magnitude) along 32 equally spaced sectors. The data on velocity fields were further processed in Matlab to generate kymographs and average velocity along vertical slices of the field of view. To determine the wave time-period T, a sinusoidal curve was fitted to average velocity over time using Matlab's curve fitting toolbox. Statistical significance was tested using the two-sample Kolmogorov–Smirnov test in Matlab.

Self-propelled Voronoi simulations

Simulations were run using a custom Matlab (Mathworks) implementation of the self-propelled Voronoi model adapted from [43]. The number of cells was determined by measuring average cell

area in experimental images using ImageJ and dividing experimental confinement size by average cell area. Simulated confinement was chosen to correspond to the experimental configuration in terms of aspect ratio and size relative to cell size. Voronoi models represent cells by their center and compute their Voronoi tessellation at every simulation time-step to determine edges and vertices. At every simulation step, cell centers are moved according to the force arising from tissue energy and self-propulsion, where μ is a constant mobility factor:

$$\partial_\tau r_i = \mu F_i + f_i^s \quad (1)$$

The force $F_i = -\nabla_{r_i} E$ for cell i is determined by the change in tissue energy E from a displacement of cell center r_i, which affects cell i and its n immediate neighbors. K_A and K_P denote cell stiffness constants.

$$E = \sum_{j=i}^{i+n} \left[k_A (A_j - A_0)^2 + k_p (P_j - P_0)^2 + k_r \left(r_{ij} - \sqrt{A_0} \right)^2 \right] \quad (2)$$

The equation was adapted from [43] to include a soft-core repulsion term [44], when the distance between the centers of a cell and its neighboring one is smaller than the characteristic cell length $\sqrt{A_0}$: $k_r = 0$ for $r_{ij} > \sqrt{A_0}$. This term stabilizes the simulation when introducing boundaries of movement. $A_j - A_0$ denotes the deviation of cell area A_j from target cell area and $P_j - P_0$ the deviation of cell perimeter P_j from target cell perimeter P_0. The definition of a shape factor $p_0 = P_0/\sqrt{A_0}$ reduces the degrees of freedom, thereby simplifying the comparison between different sets of parameters, while still capturing the competition between cellular contractility and junctional adhesion. The self-propulsive velocity $v_i = v_0 n_i$ points in the direction of cell polarization $n_i = (\cos\theta_i, \sin\theta_i)$. Cell polarization θ_i aligns with the direction of cell displacement ϕ_i according to the equation:

$$\partial_\tau \theta_i = \frac{-1}{t} (\theta_i - \phi_i) + \eta_i \quad (3)$$

Here, τ is the self-alignment time and η_i the white noise. To simulate the PDMS channel confining the cellular monolayer, slip (no-penetration) boundary conditions were implemented at the boundaries as follows: $x|y| = 0$ and $x|y| = L_x$, as well as $y|x| = 0$ and $y|x| = L_y$. Specifically, when the computed displacement of a cell $\partial_\tau r_i$ would have resulted in passing the channel boundaries, the cell was displaced by the tangential component, but not the normal component with respect to the boundary. Simulated confinement was chosen to correspond to the experimental configuration in terms of aspect ratio and size relative to cell size. In vertex models, jamming and unjamming transitions are defined by the shape factor P_0 and self-propulsive velocity v_0. Furthermore, the coordination of movement in flocks of cells is determined the self-alignment time τ. These parameters were set to $p_0 = 3.7$ and $\tau \leq 0.25$ sec to simulate unjammed, liquid flock-like movement. $A_0 = 807.7\ \mu m^2$. Therefore, 9905 cells were simulated to cover 8 mm^2 of confinement. k_r is kept fixed, *i.e.* $k_r = 1\ \mathbf{sec}^{-1}$ and k_A and k_P are varied, along with v_0, to match the experimental phenomenology.

Results and discussion

Wave formation of unjammed collectives

Madine-Darby canine kidney (MDCK) cells have been broadly used to study epithelial migration dynamics [39, 45, 46]. In previous work, we showed that a specific MDCK type II strain (PM-YFP), stably expressing the fluorescent reporter growth-associated protein 43-yellow fluorescent protein (GAP43-YFP) localized at the plasma membrane, presented delayed jamming dynamics compared to the wild type (WT) type II strain counterpart [39]. These 2 cell lines were seeded at high density in Lx =8 mm long and Ly = 1 mm wide channels to impose geometrical constrain, and after 20 h to ensure the maturation of cell–cell junctions the collective motion of monolayers was recorded for 40 h and analyzed with cell image velocimetry (CIV). Figure 1a shows representative BF microscopy images from the center of the channel and the corresponding CIV directionality frames. While no coherent motion was detected in the WT monolayers, the PM-YFP movement was coordinated along the vertical axis (y) of the geometrical confinement: clusters of cells collectively moved in the direction of the horizontal axis (x) and waves of coordinated migration occurred. To quantify these observations, cell velocity for a vertical segment of the channel (white dashed lines) was averaged. The representation of the x-velocity over time (Fig. 1b) showed an oscillatory behavior along the channel for the PM-YFP cells, while the WT counterparts move very little and without any evident oscillation. We previously reported that WT cells jam earlier (around 20 h) in epithelial monolayers and their velocity is highly reduced compared to the PM-YFP cells [39]. We then corroborate this observation comparing 2 different lines of MCF10A breast cancer epithelial cells: the original line (EV) and a line overexpressing the endocytic protein RAB5A, where the cell jamming is reverted and coordinated motility is increased [40]. Consistent with what we observed in the MDCK cells, regions with high migration coherence and oscillatory behavior of the x-velocity characterized the unjammed MCF10A-RAB5A (Fig. S1).

To better understand how this wave-like motility was propagating along the channels we used a vertex model coupled with self-propelled Voronoi diagram [43, 44, 47]. In vertex models, jamming and unjamming transitions are defined by the shape factor P_0 and the self-propulsive velocity v_0. Furthermore, the coordination of movement in clusters of cells is determined by the self-alignment time τ [43]. Two sets of parameters were selected to compare the behavior of jammed and unjammed cells (Fig. 1c and d). The self-propulsive velocity was set to $v_0 = 1$ for both cell types. At $P_0 = 3.1$ and $\tau = \infty$ cell type 1 was chosen to fall into the range of jammed, solid-like behavior. The same parameters were set to $P_0 = 3.7$ and $\tau = 0.25$ sec for cell type 2 well within the domain of unjammed dynamics. As shown in **Fig. 1c** and **d**, the model was able to recapitulate the experiments performed *in vitro* and captured the waves-like movement propagation of cells in the unjammed phase (cell type 2) compared to the jammed phase (cell type 1). The cells formed pronounced waves in the x-direction. Nonetheless, experimentally observed dynamics were not replicated in their exact form by the simulations: while oscillations were clearly present, their spatial and temporal dynamics did not match the experimental outcomes. In experiments, PM-YFP cells formed multi-nodal oscillations, like a standing wave pattern along the x-axis. Simulations produced global oscillations, where waves travel along the entire channel. To simulate the multimodal oscillation behavior detected in the *in vitro* experiments, we combined the parameters from the sets $v_0 = 0.5, 1, 2\ \mu$m/sec; $P_0 = 3.1, 3.5, 3.7, 3.9, 4.1$; and $\tau = 0.125, 0.25, 0.5$ sec with no positive results (see Fig. 2c and d). Qualitatively, also a difference in cell shape was observed between experiments and simulations: in areas of high cell density, where clusters of cells moving in opposite directions collide, PM-YFP cells were more elongated that the simulated Voronoi cells. When increasing the shape factor P_0

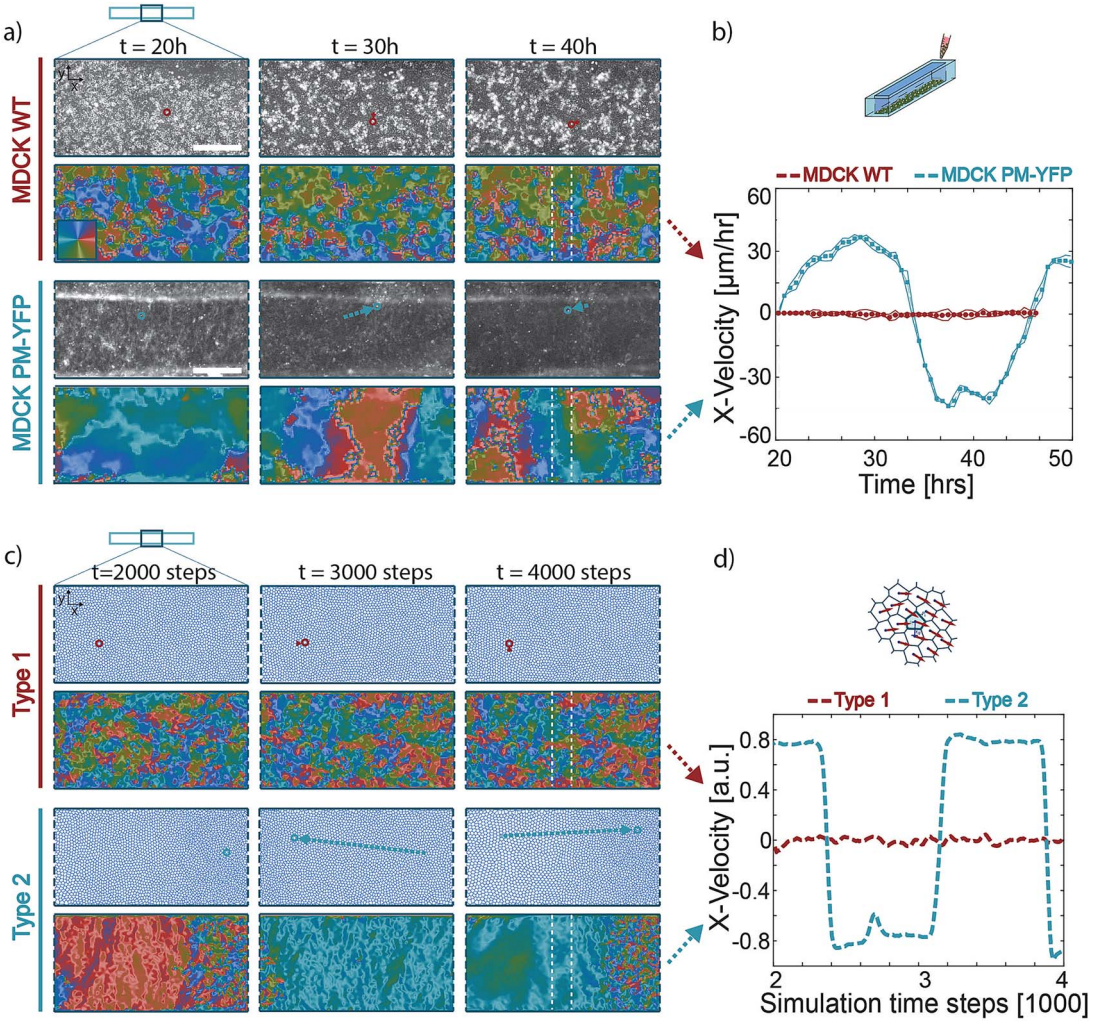

Figure 1. Wave formation in rectangular channels occurs for cells in the unjammed state in experiments and simulations. Experiments: (a) representative images of cell distribution (grey-scale, top rows) and velocity direction correlation as computed by CIV analysis (pseudo-color, bottom rows) of MDCK WT and MDCK PM-YFP. The time of experiment duration is displayed on top of the images. Displacement of a cell is reported by circles and arrows. The scale bar corresponds to 500 μm. (b) Velocity in x-direction (parallel to the long axis of confinement), quantified from CIV, in the center of the eld of view (white dashed lines) for MDCK WT and PM-YFP. Data are reported means ± standard deviations, n = 3. Simulations: (c) representative images of simulated Voronoi cells (top rows) and velocity direction correlation (pseudo-color, bottom rows) of type 1 and type 2 cells. The number of simulation time steps is displayed on top of the images. Displacement of a cell is reported by circles and arrows. (d) Velocity in x-direction (parallel to the long axis of confinement) in the center of the eld of view (white dashed lines). The parameters used in the simulations are stated in the text, other parameters are $k\_A \cong 1.66 \mathrm{sec}^{-2}\mu m^{-2}$ and $k_p = 0.665$.

allowing cells to elongate more, the energy barrier for neighbor exchanges was decreased. For $P_0 > 4$, this prevented cell cluster behavior independent of self-alignment time τ [43]. While in the simulations comparable cell areas and frequency fractions were observed for cell type 1 and 2 (Fig. S2a), the comparison between the data from experiments and simulations for PM-YFP cells showed a higher standard deviation in the experimental data (Fig. S2b). As no combination of the simulation parameters could be found to induce multi-nodal oscillations seen in the experiments, the model should be addressed to improve agreement. Speculatively this could be achieved by incorporating junctional remodeling through an addition term in the energy equation or by using a vertex model that tracks the junctions explicitly. Alternatively, simulations could also incorporate the cells dynamics in the third dimension, allowing cells to undergo large area changes that are missing in the vertex model. Moreover, a particle-based model could be implemented to see if the wave dynamics is better captured [11]. Despite these discrepancies, the model remains valuable as it demonstrates that specific parameter changes, representing cell "stiffness" and collective realignment, can induce wave-like movements like experimental observations. It also confirms that cell-intrinsic properties are more influential than external guidance cues, such as micro-gratings (contact guidance), in wave formation. Finally, the model can guide future experimental designs and help prioritize which aspects of cell behavior to investigate further.

Impact of confinement width on wave formation

It was previously reported that, in *in vitro* and *in vivo* systems, the wavelength patterns arise in confined geometries [16–18, 48, 49], with wavelength and period characterized by spatial and temporal consistency. In small areas of confinement, the period of waves correlates with the length of the smallest dimension of confinement [31, 32]. To determine whether oscillations in larger areas of confinement were fundamentally of the same nature, PM-YFP cell behavior was observed culturing them in

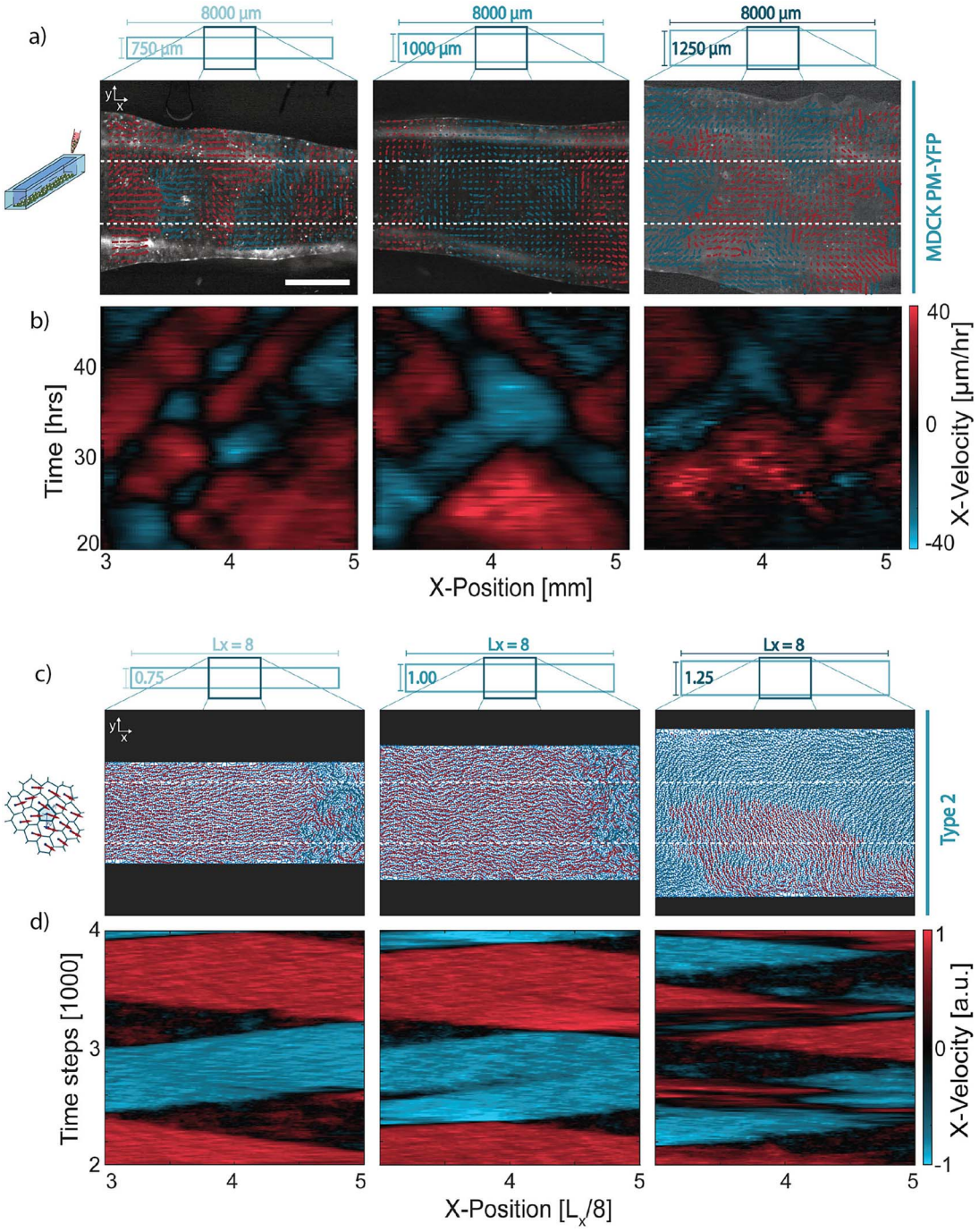

Figure 2. Visualization of the impact of variations in confinement width on wave formation. Experiments: (a) representative images of MDCK PM-YFP in confinements measuring Ly = 750 μm, Ly = 1000 μm, and Ly = 1250 μm in width. Arrows indicate the direction of movement, where arrows with a positive x-velocity component are red and arrows with a negative x-velocity component are blue. The scale bar corresponds to 500 μm. (b) Representative kymographs of the average x-velocity over time. Velocity was averaged vertically for the area indicated by the white dashed lines in a. simulations: (c) representative images of simulated Voronoi cells (type 2) in confinements of aspect ratios corresponding to experiments (0.75:8, 1:8, and 1.25:8). Arrows indicate the direction of movement, where arrows with a positive x-velocity component are red and arrows with a negative x-velocity component are blue. (D) Representative kymographs of the average x-velocity over time. Velocity was averaged vertically for the area indicated by the white dashed lines in c.

channels of three different widths Ly = 750 μm, Ly = 1000 μm, and Ly = 1250 μm, respectively, while Lx = 8 mm was kept constant. Analogously, the aspect ratio of confinement in the simulations was adjusted to 0:75×8, 1:00×8, and 1:25×8. To keep cell density constant, the number of simulated cells was modified to 7429, 9905, and 12 381, respectively. As reported by the kymographs in Fig. 2, both in experiments (panels a and b) and in simulation (panels c and d), wave formation was visible in all channels, and the width of waves increased with that of the channels, at least for Ly = 750 μm, Ly = 1000 μm. This observation was further confirmed by the quantification of the wave width (Fig. S3). For larger channels, the disappearance of coordinated clusters, not spanning the entire channel's width, makes any conclusion very hard to draw. As a matter of fact, at Ly = 1250 μm, waves no

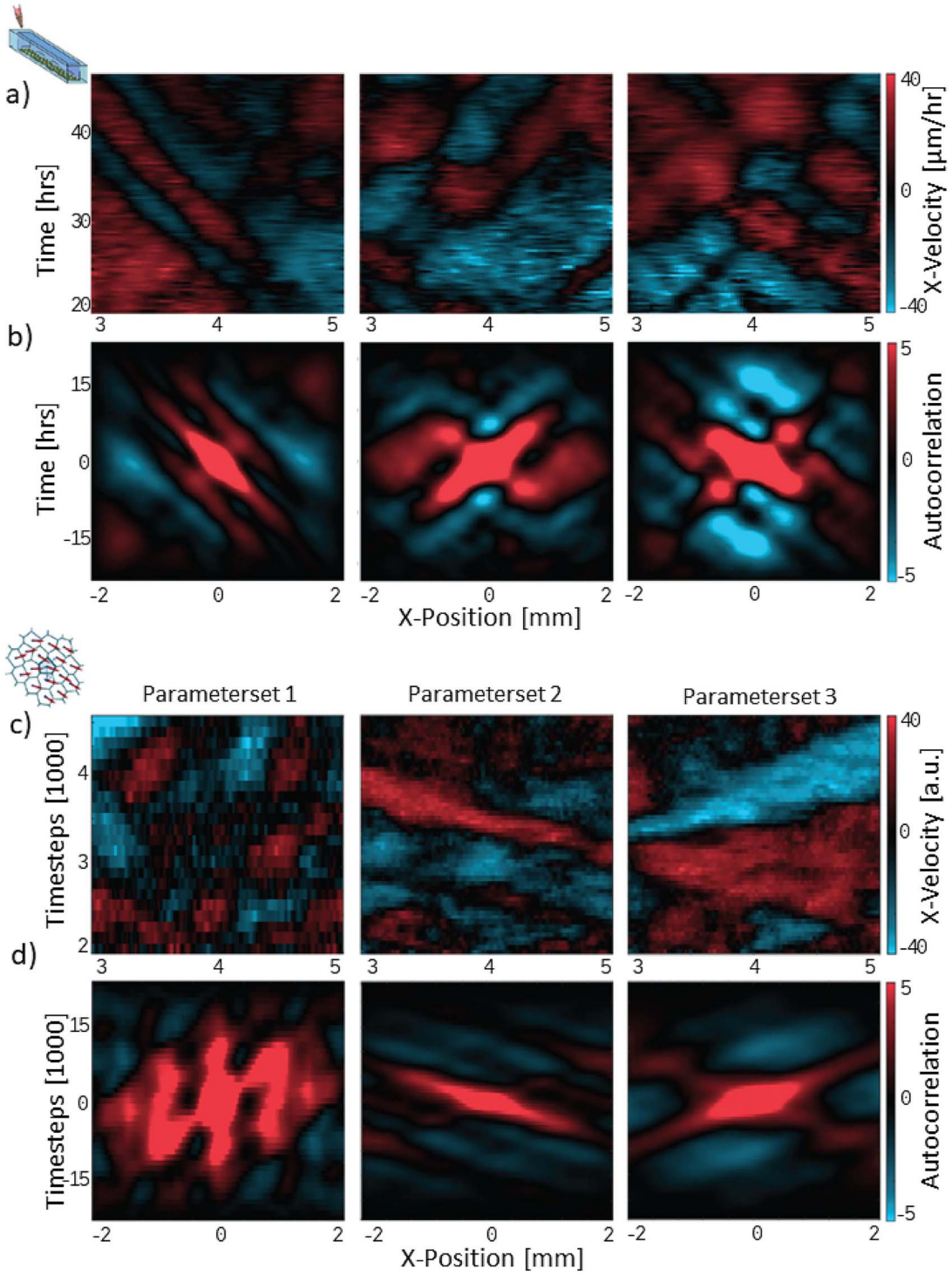

Figure 3. Visualization of the wave formation dynamics in 750 μm confinement width channels. (a) Kymographs of different experiments carried out within the same channel. The typical parallel stripe structures with nodal points are visible. (b) the VACF from the kymographs in panel (a) are displayed showing the time and space periodicity, wavelengths quantifications: 0.37 mm $\pm$ 0.07 mm, 0.49 mm $\pm$ 0.03 mm and 0.51 mm $\pm$ 0.02 mm for left, middle and right panel, respectively. (c) Kymographs generated from the Voronoi model dynamics. In the transient initial part of the dynamics the oscillatory behavior reproduces the experimental features, before entering the global oscillating phase shown in Fig. 2d. The appearance and duration of their phase depends on the values of the parameters, an entire range of parameters indeed allows the formation of nodal oscillating clusters of cells: Parameter set 1: $v_0 = 0.13, k_A = 2.613\text{sec}^{-2}\mu m^{-2}, k_P = 0.86\text{sec}^{-2}, \tau = 0.1$ sec in the first panel, Parameterset 2: $v_0 = 0.1, k_A = 2.613\text{sec}^{-2}\mu m^{-2}$, $k_P = 0.86\text{sec}^{-2}, \tau = 0.125$ sec in the second panel and Parameterset 3: $v_0 = 0.1, k_A = 2.613\text{sec}^{-2}\mu m^{-2}, k_P = 0.86\text{sec}^{-2}, \tau = 0.175$ sec in the last panel. (d) VACF calculated from the kymographs in (c), wavelengths quantifications: 0.44 mm $\pm$ 0.08 mm, 0.57 mm $\pm$ 0.05 mm and 0.52 mm $\pm$ 0.02 mm for left, middle and right panel, respectively.

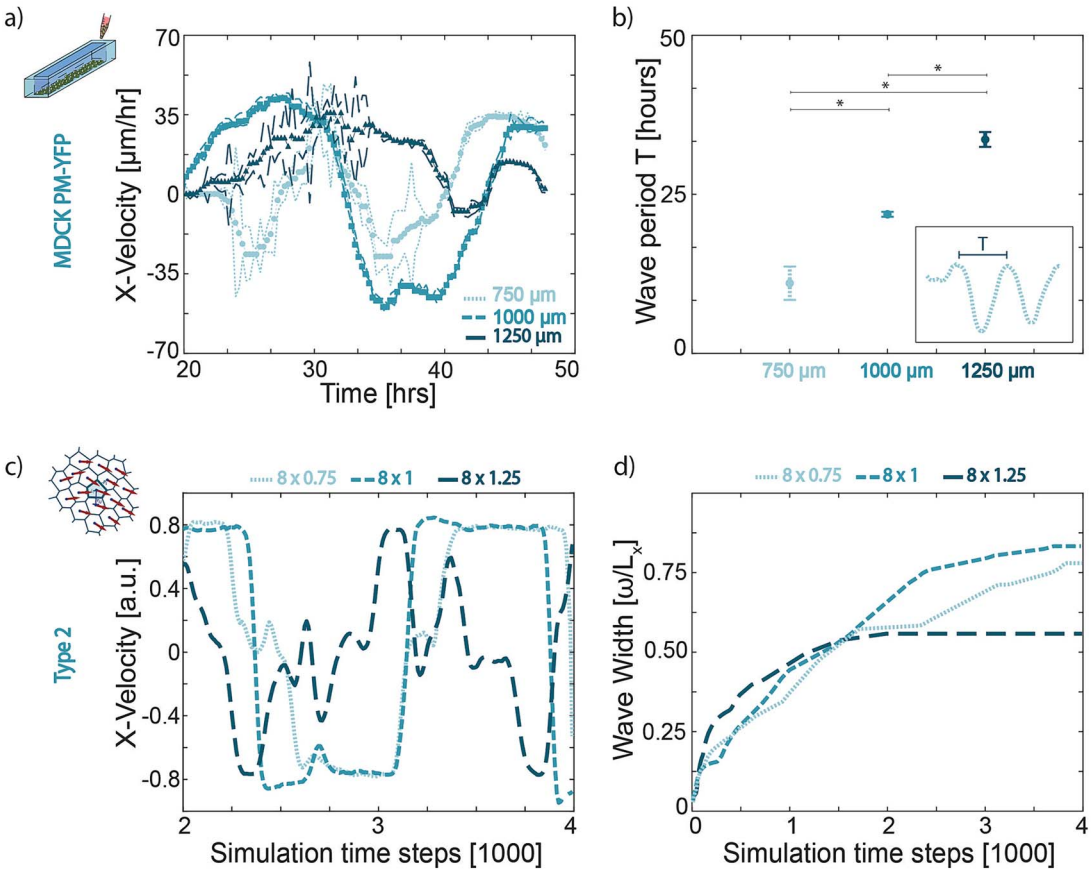

Figure 4. Quantification of the impact of variations in confinement width on wave formation. Experiments: a) velocity in x-direction (parallel to the long axis of confinement) of MDCK YFP, quantified from CIV, in the center of the field of view (see white dashed lines in Fig. 1 for confinements measuring Ly = 750 μm, Ly = 1000 μm, and Ly = 1250 μm in width. Data are represented as means ± standard deviations; n = 3. b) Wave period over confinement width, quantified from CIV. Each data point corresponds to at least three experiments. $* = P < 0.05$. Simulations: c) velocity in x-direction (parallel to the long axis of confinement), averaged over the center of the field of view (see white dashed lines in Fig. 1 for confinement aspect ratios of 0.75 × 8, 1 × 8, and 1.25 × 8. d) Ratio of wave width to the length of confinement lx over time for different confinement aspect ratios.

longer covered the entire vertical axis of confinement. In the experiments with Ly = 750 μm, Ly = 1000 μm, clusters traveling in opposing directions pushed past one another. This is particularly clear in the kymographs, where red and blue streaks appeared broken up (Fig. 2b) closely resembling the patterns displayed in ref. [33]. The clusters dynamics indeed is characterized by a velocity with periodic oscillations in space. However, these alternating phases fade out if the channel width is increased (Ly = 1250 μm). The spatiotemporal disparity between the oscillating dynamics in the simulated channels and the real ones is evident in Fig. 2d. Notably, in the simulated channels, nodal points appeared to be entirely absent, and the slopes of the red and blue stripes, which signify collective motion in a specific direction, were reversed. Conversely, in Fig. 2b, the streaks appeared to be parallel and separated in lozenges by vertical nodal black lines. However, a close inspection of the dynamics revealed that the global oscillations observed in simulations represented the asymptotic stationary regime of cell movement in confinement. While the cells velocity initialization was random, the self-alignment constraint caused the transient appearance of structures which resemble those observed in the experiments, with oscillations which had local nodal character instead of spanning the entire channel's size. The global oscillations that eventually emerged were a consequence of the global realignment of cells within a wave: after a single wave reached the channel's boundaries, it bounced back. This is shown in Fig. 3, where the kymographs from the experiments (panel a) resembled those obtained from simulations (panel c). These local patterns did not last for long, and the global oscillatory behavior took over after some time. The transition to the stationary regime depended on the values of the parameters used, as it is described in the caption of Fig. 3. Remarkably, the distance between waves increased with channel width both in the experiments and in the simulations. The quantitative analysis of the kymograph was achieved by calculation of the 2D velocity autocorrelation function (VACF) $(g(\delta x, \delta t) = < v(x,t)\, v(x+\delta x, t+\delta t) >$ [43]. In Fig. 3b the calculation of the experimental kymograph VACF yielded the peak-like structure where spatial and temporal periodicity can be assessed: the time-period is $T \cong 5\ h$, whereas the space period is $\lambda \cong 0.5\ mm$. In Fig. 3d the VACF is displayed for the corresponding upper panels. It is immediately clear how the phenomenology of the VACF mirrored qualitatively the experimental VACF in panel b, with a quantitative agreement of the spatial period.

The quantification of x-velocity in experiments demonstrated the impact of confinement width on wave formation (Fig. 4a). The number of x-velocity peaks inversely correlated with increasing confinement width Ly and was reduced from three peaks for Ly = 750 μm to a single peak for Ly = 1250 μm. Furthermore, the x-velocity curve for Ly = 1250 μm did not follow a clean sinusoidal shape, as in the thinner channels, which is a result of clusters moving opposing directions at the same x-position. An opposite

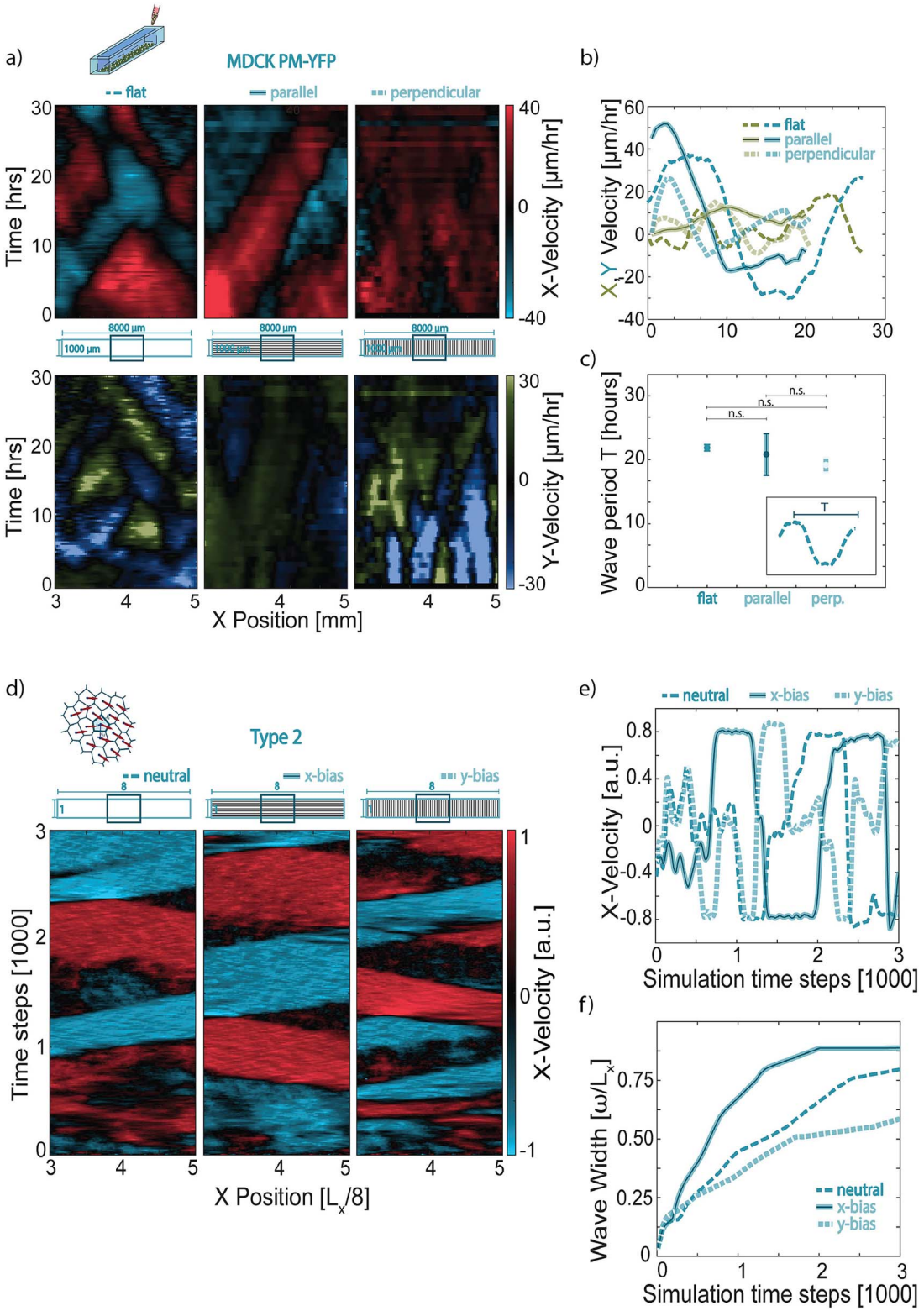

Figure 5. Impact of substrate micro-pattern on wave formation in rectangular confinement. Experiments: (a) representative kymographs of the average x-velocity (top row) and y-velocity (bottom row) over time for MDCK PM-YFP in rectangular confinement on a flat substrate, a substrate with microgrids parallel to the long axis of confinement, and microgrids perpendicular to the long axis of confinement. Velocity was averaged vertically (analogous to Fig. 2). (b) Quantification of average x-velocity (blue) and y-velocity (green) for flat, parallel micropattern, and perpendicular micropattern substrates. Velocity was averaged over the center of the field of view (see Fig. 1). (c) Wave period, quantified from CIV. Each data point corresponds to three experiments. n.s. = not significant. Simulations: (d) representative kymographs of the average x-velocity over time for cells in rectangular confinement for a neutral configuration, a bias towards movement in y-direction and a bias towards movement in x-direction. Biases were chosen to correspond to micropatterned substrates in experiments. Velocity was averaged vertically (analogous to Fig. 2). (e) Quantification of average x-velocity for the neutral, x-biased (parallel) and y-biased (perpendicular) simulation configurations. (f) Ratio of wave width to the length of confinement lx over time for different substrate pattern configurations as represented by movement biases.

trend was observed for the wave period T. As shown in Fig. 4b, between Ly =750 μm and Ly = 1250 μm, the time-period triples from an average of 661 min for T_{750} to an average of 2017 min for T_{1250}, respectively. All these results indicated that wave formation in larger channels followed the same time-period to size correlation as in smaller channels. The results of X-velocity in simulated channels of varying aspect ratios instead highlighted a striking difference between aspect ratios 1.00 × 8 and 1.25 × 8. Conversely to what was measured in the experiments (Fig. 4a), in the wider confinement the wave pattern was lost and instead, smaller fluctuations appeared superimposed on the global oscillation (Fig. 4**c**). As shown in Fig. 4d, rather than generating differences in the wave frequency, varying channel width in simulations changed the fraction of the channel occupied by the global wave and the time it took to form it. Interestingly, the wave initially grew slightly faster in the channel with aspect ratio 1.25 × 8, but it reached a plateau earlier compared to the waves in channels of aspect ratios 0.75 × 8 and 1.00 × 8.

Impact of microtopography on wave formation

Several studies demonstrated that micropatterned gratings on substrates directed single and collective cell migration and increased cell velocity [50–53]. They also can converge with other guidance mechanisms, such as the movement towards cell-free areas, thus accelerating wound healing [41, 54]. To investigate the interplay between gratings-induced contact guidance and geometric confinement, cells were placed on substrates patterned with microgrooves of 1 μm width, depth, and separation within PDMS channels.

The confinement dimensions were kept equal at Ly = 1000 μm and Lx = 8 mm and the anisotropic topographies were carefully aligned parallel or perpendicular to the long axis of geometric confinement. Representative kymographs of cell velocity in x-direction (top) and y-direction (bottom) (Fig. 5a) and their quantification (Fig. 5b) showed that parallel microgrooves (gratings) decreased the time to wave appearance and attenuated oscillations in the y-direction. Conversely, perpendicular microgrooves (gratings) decreased the x-velocity amplitude of waves but did not hamper wave formation. Finally, no significant difference in wave time-period was observed between flat and patterned substrates, suggesting that the size of confinement dominated as a mechanical cue for wave formation (Fig. 5c). Since gratings guide cell motion by imposing a direction on cytoskeletal fiber polymerization within protrusions [55], these results indicated that confinement from surrounding cells is more relevant in directing cytoskeleton polymerization than microgrooves.

To simulate cell migration on microgrooves, a tissue force bias b = 0.1 in the direction of grooves was implemented. Thereby, cells were more inclined to move in the x-direction for simulated parallel grooves (x-bias) and the y-direction for simulated perpendicular grooves (y-bias), respectively. Bias b was set to the largest value possible without causing instabilities in cell displacement. Corresponding to experiments, the confinement aspect ratio was set to 1 × 8 for all cases. Kymographs of x-velocity simulations and quantifications are reported in Fig. 5d and e. To illustrate initial differences in wave formation, plots start at simulation time step 0. Like parallel grooves in experiments, the x-bias reduced the time to initial wave formation. The y-bias did not impede wave formation but induced additional fluctuations in x-velocity. Biases do not change the velocity or time-period waves. However, it is interesting to notice how the global oscillations constituted the asymptotic stationary regime also in presence of geometrical biases, while the initial transient regimes were dominated by sustained local oscillation. As shown in Fig. 5f, the x-bias increases wave width with respect to the channel length Lx, while a y-bias reduces wave width in comparison to the neutral configuration.

Altogether, these results indicated that confinement-induced wave formation occurred independently of contact guidance cues from microgrooves. Nonetheless, the convergence of contact guidance cues with confinement can augment wave formation when aligned and limit wave formation when misaligned.

Conclusion

In this work we studied oscillatory motion in smaller areas of confinement, and we identified the relationship between monolayer maturation induced jamming and wave formation. Combining experimental data and simulations, we demonstrated that collective migratory oscillations under large geometrical confinement depended on the jamming state of the confined monolayer. MDCK PM-YFP cells, characterized by delayed jamming [39], formed collective oscillations under geometrical confinements, whereas jammed MDCK WT cells did not. We were able to reproduce similar results by self-propelled Voronoi simulations comparing cells with solid-like and fluid-like behavior. Analogous to small areas of confinement, wave frequency was determined by the length of confinement along the short axis. Between Ly =750 μm and Ly =1250 μm, the wave time-period tripled. Both in experiments and simulations, waves ceased to cover the entire vertical axis of confinement at Ly =750 μm, indicating that this may be a critical length scale for wave formation for the duration of experiments here performed.

We also explored the role of topographical features in wave formation dynamics using different microscale surface structures. We found that wave formation under confinement can occur independently of the presence of microtopography. Microgrooves oriented perpendicular to the long axis of confinement had no effect on the wave time-period. Conversely, microgrooves parallel to the long axis of confinement impacted on wave propagation speed and directionality, accelerating wave formation, and reducing vertical motion. SPV simulations fully supported the phenomenon of wave formation under confinement and in the early dynamic stage of the system the simulated patterns closely resembled the sustained nodal oscillatory dynamics detected in the experiments.

Supplementary data

Supplementary data is available at *INTBIO Journal* online.

Funding

F.M.P. and S.L. are supported by funding from ETH grant ETH-07 17–1 Namaste.

Conflict of interest

None declared.

References

1. Puliafito A, Hufnagel L, Neveu P. *et al.* Collective and single cell behavior in epithelial contact inhibition *Proc Natl Acad Sci U S A*. 2012;**109**:739–44.
2. George M, Bullo F, Campas O. Connecting individual to collective cell migration *Sci Rep*. 2017;**7**:9720.

3. Friedl P, Gilmour D. Collective cell migration in morphogenesis, regeneration and cancer *Nat Rev Mol Cell Biol*. 2009;**10**:445–57.
4. Friedl P, Mayor R. Tuning collective cell migration by cell-cell junction regulation *Cold Spring Harb Perspect Biol*. 2017;**9**: a029199.
5. Friesen DE, Craddock TJA, Kalra AP. *et al.* Biological wires, communication systems, and implications for disease *Biosystems*. 2015;**127**:14–27.
6. Vedula SR, Leong MC, Lai TL. *et al.* Emerging modes of collective cell migration induced by geometrical constraints *Proc Natl Acad Sci U S A*. 2012;**109**:12974–9.
7. Janmey PA, Miller RT. Mechanisms of mechanical signaling in development and disease *J Cell Sci*. 2011;**124**:9–18.
8. Guillot C, Lecuit T. Mechanics of epithelial tissue homeostasis and morphogenesis *Science*. 2013;**340**:1185–9.
9. Tambe DT, Hardin CC, Angelini TE. *et al.* Collective cell guidance by cooperative intercellular forces *Nat Mater*. 2011;**10**:469–75.
10. Zaritsky A, Welf ES, Tseng YY. *et al.* Seeds of locally aligned motion and stress coordinate a collective cell migration *Biophys J*. 2015;**109**:2492–500.
11. Tarle V, Ravasio A, Hakim V. *et al.* Modeling the finger instability in an expanding cell monolayer *Integr Biol (Camb)*. 2015;**7**: 1218–27.
12. Inoue Y, Tateo I, Adachi T. Epithelial tissue folding pattern in confined geometry *Biomech Model Mechanobiol*. 2020;**19**:815–22.
13. Rolli CG, Nakayama H, Yamaguchi K. *et al.* Switchable adhesive substrates: revealing geometry dependence in collective cell behavior *Biomaterials*. 2012;**33**:2409–18.
14. Blin G, Wisniewski D, Picart C. *et al.* Geometrical confinement controls the asymmetric patterning of brachyury in cultures of pluripotent cells *Development*. 2018;**145**:dev166025.
15. Sen D, Voulgaropoulos A, Keung AJ. Effects of early geometric confinement on the transcriptomic profile of human cerebral organoids *BMC Biotechnol*. 2021;**21**:59.
16. Rupprecht JF, Ong KH, Yin JM. *et al.* Geometric constraints alter cell arrangements within curved epithelial tissues *Mol Biol Cell*. 2017;**28**:3582–94.
17. Dicko M, Saramito P, Blanchard GB. *et al.* Geometry can provide long-range mechanical guidance for embryogenesis *PLoS Comput Biol*. 2017;**13**:e1005443.
18. Szabo A, Melchionda M, Nastasi G. *et al.* In vivo confinement promotes collective migration of neural crest cells *J Cell Biol*. 2016;**213**:543–55.
19. Doolin MT, Moriarty RA, Stroka KM. Mechanosensing of mechanical confinement by mesenchymal-like cells *Front Physiol*. 2020;**11**:365.
20. Ilina O, Gritsenko PG, Syga S. *et al.* Cell-cell adhesion and 3D matrix confinement determine jamming transitions in breast cancer invasion *Nat Cell Biol*. 2020;**22**:1103–15.
21. Irimia D, Toner M. Spontaneous migration of cancer cells under conditions of mechanical confinement *Integr Biol*. 2009;**1**:506–12.
22. Atia L, Fredberg JJ, Gov NS. *et al.* Are cell jamming and unjamming essential in tissue development? *Cells Dev*. 2021;**168**:203727.
23. Park JA, Atia L, Mitchel JA. *et al.* Collective migration and cell jamming in asthma, cancer and development *J Cell Sci*. 2016;**129**: 3375–83.
24. Kim JH, Pegoraro AF, Das A. *et al.* Unjamming and collective migration in MCF10A breast cancer cell lines *Biochem Biophys Res Commun*. 2020;**521**:706–15.
25. Garcia S, Hannezo E, Elgeti J. *et al.* Physics of active jamming during collective cellular motion in a monolayer *Proc Natl Acad Sci U S A*. 2015;**112**:15314–9.
26. Camley BA, Rappel WJ. Physical models of collective cell motility: from cell to tissue *J Phys D Appl Phys*. 2017;**50**:113002.
27. Zaritsky A, Kaplan D, Hecht I. *et al.* Propagating waves of directionality and coordination orchestrate collective cell migration *PLoS Comput Biol*. 2014;**10**:e1003747.
28. Petitjean L, Reffay M, Grasland-Mongrain E. *et al.* Velocity fields in a collectively migrating epithelium *Biophys J*. 2010;**98**: 1790–800.
29. Blanch-Mercader C, Yashunsky V, Garcia S. *et al.* Turbulent dynamics of epithelial cell cultures *Phys Rev Lett*. 2018;**120**: 208101.
30. Doxzen K, Vedula SRK, Leong MC. *et al.* Guidance of collective cell migration by substrate geometry *Integr Biol*. 2013;**5**:1026–35.
31. Deforet M, Hakim V, Yevick HG. *et al.* Emergence of collective modes and tri-dimensional structures from epithelial confinement *Nat Commun*. 2014;**5**:3747.
32. Peyret G, Mueller R, d'Alessandro J. *et al.* Sustained oscillations of epithelial cell sheets *Biophys J*. 2019;**117**:464–78.
33. Petrolli V, Le Goff M, Tadrous M. *et al.* Confinement-induced transition between wavelike collective cell migration modes *Phys Rev Lett*. 2019;**122**:168101.
34. Yu J, Cai P, Zhang X. *et al.* Spatiotemporal oscillation in confined epithelial motion upon fluid-to-solid transition *ACS Nano*. 2021;**15**:7618–27.
35. Reig G, Pulgar E, Concha ML. Cell migration: from tissue culture to embryos *Development*. 2014;**141**:1999–2013.
36. Haeger A, Wolf K, Zegers MM. *et al.* Collective cell migration: guidance principles and hierarchies *Trends Cell Biol*. 2015;**25**: 556–66.
37. Hegarty-Cremer SGD, Simpson MJ, Andersen TL. *et al.* Modelling cell guidance and curvature control in evolving biological tissues *J Theor Biol*. 2021;**520**:110658.
38. Zacharias DA, Violin JD, Newton AC. *et al.* Partitioning of lipid-modified monomeric GFPs into membrane microdomains of live cells *Science*. 2002;**296**:913–6.
39. Lohmann S, Giampietro C, Pramotton FM. *et al.* The role of Tricellulin in epithelial jamming and unjamming via segmentation of Tricellular junctions *Adv Sci*. 2020;**7**:2001213.
40. Malinverno C, Corallino S, Giavazzi F. *et al.* Endocytic reawakening of motility in jammed epithelia *Nat Mater*. 2017;**16**: 587–96.
41. Pramotton FM, Robotti F, Giampietro C. *et al.* Optimized topological and topographical expansion of epithelia *ACS Biomater Sci Eng*. 2019;**5**:3922–34.
42. Milde F, Franco D, Ferrari A. *et al.* Cell image velocimetry (CIV): boosting the automated quantification of cell migration in wound healing assays *Integr Biol (Camb)*. 2012;**4**: 1437–47.
43. Giavazzi F, Paoluzzi M, Macchi M. *et al.* Flocking transitions in confluent tissues *Soft Matter*. 2018;**14**:3471–7.
44. Barton DL, Henkes S, Weijer CJ. *et al.* Active vertex model for cell-resolution description of epithelial tissue mechanics *PLoS Comput Biol*. 2017;**13**:e1005569.
45. Kim M, Jang H, Park Y. Study on the expansion dynamics of MDCK epithelium by interstitial flow using a traction force-measurable microfluidic Chip *Mater (Basel)*. 2021;**14**:935.
46. Angelini TE, Hannezo E, Trepat X. *et al.* Glass-like dynamics of collective cell migration *Proc Natl Acad Sci U S A*. 2011;**108**:4714–9.
47. Bi DP, Yang XB, Marchetti MC. *et al.* Motility-driven glass and jamming transitions in biological tissues *Phys Rev X*. 2016;**6**: 021011.
48. Lecuit T, Lenne PF. Cell surface mechanics and the control of cell shape, tissue patterns and morphogenesis *Nat Rev Mol Cell Biol*. 2007;**8**:633–44.
49. Zhang Y, Xu G, Wu J. *et al.* Propagation dynamics of electrotactic motility in large epithelial cell sheets *iScience*. 2022;**25**:105136.

50. Dalton BA, Walboomers XF, Dziegielewski M. *et al*. Modulation of epithelial tissue and cell migration by microgrooves *J Biomed Mater Res*. 2001;**56**:195–207.
51. Clark P, Connolly P, Moores GR. Cell guidance by micropatterned adhesiveness in vitro *J Cell Sci*. 1992;**103**: 287–92.
52. Londono C, Loureiro MJ, Slater B. *et al*. Nonautonomous contact guidance signaling during collective cell migration *Proc Natl Acad Sci U S A*. 2014;**111**:1807–12.
53. Kim DH, Han K, Gupta K. *et al*. Mechanosensitivity of fibroblast cell shape and movement to anisotropic substratum topography gradients *Biomaterials*. 2009;**30**:5433–44.
54. Lee G, Atia L, Lan B. *et al*. Contact guidance and collective migration in the advancing epithelial monolayer *Connect Tissue Res*. 2018;**59**:309–15.
55. Lee K, Kim EH, Oh N. *et al*. Contribution of actin filaments and microtubules to cell elongation and alignment depends on the grating depth of micrograting *J Nanobiotechnology*. 2016;**14**:35.